

RESEARCH ARTICLE



Monolith/Hydrogel composites as triamcinolone acetonide carriers for curing corneal neovascularization in mice by inhibiting the fibrinolytic system

Cixin Huang^{a,b,c}, Xia Qi^{b,d}, Huilin Chen^{a,b,c}, Wei Chao^{b,d}, Xiaolin Qi^{b,c,d} ,
Hongwei Wang^{b,d} and Hua Gao^{b,c,d}

^aMedical College, Qingdao University, Qingdao, China; ^bState Key Laboratory Cultivation Base, Shandong Provincial Key Laboratory of Ophthalmology, Eye Institute of Shandong First Medical University, Qingdao, China; ^cEye Hospital of Shandong First Medical University, Jinan, China; ^dSchool of Ophthalmology, Shandong First Medical University, Jinan, China

ABSTRACT

Corneal neovascularization is a serious corneal pathological change caused by various factors. The drug delivery system is of great significance for the effective treatment of corneal neovascularization. Herein, we developed and characterized a monolith/hydrogel composite as the triamcinolone acetonide (TA) carrier for curing corneal neovascularization. The composite was prepared by photo-initiated free radical polymerization of multi-methacrylate substituted dodecamine organic molecular cage and post-modified by the sequential photo-initiated free radical polymerization of acrylated gelatin. The globular morphology and structural property of as-prepared composites were evaluated by scanning electron microscopy, Fourier-transform infrared spectroscopy and solid-state cross polarization magic angle spinning carbon-13 nuclear magnetic resonance. Then swelling ratio and the TA loading capacity were investigated then. Compared with gelatin hydrogel, the composites exhibited a decreased swelling ratio and an improved loading capacity. With good biocompatibility, the composite can sustainably release TA for up to 28 days, and effectively inhibit corneal neovascularization with an alkali burn-induced corneal neovascularization model. Additionally, tandem mass tags-labeled quantitative proteomics were performed to identify differentially expressed proteins between vascularized and devascularized corneas. The Kyoto Encyclopedia of Genes and Genomes enrichment analysis revealed that the inhibition process could be primarily linked to the fibrinolytic system. These results demonstrated the potential of monolith/hydrogel composites as delivery systems in the therapy for biomedical diseases.

ARTICLE HISTORY

Received 23 September 2021
Revised 22 November 2021
Accepted 29 November 2021

KEYWORDS

Hydrogel; monolith; composite; corneal neovascularization; drug delivery system

1. Introduction

Corneal neovascularization is a category of pathological angiogenesis that threatens the vision and even causes blindness (Ueta et al., 2019; Cho et al., 2020). Pro-angiogenic factors and anti-angiogenic factors are two counterbalancing systems that determine the formation of new blood vessels (Senturk et al., 2016; Wang et al., 2019). Inflammation and other causes can break the balance of the two systems, consequently resulting in corneal neovascularization (Senturk et al., 2016). Cornea transplantation, laser therapy, steroids, anti-vascular endothelial growth factor (VEGF) agents, insulin receptor substrate-1 proteins, matrix metalloproteinase inhibitors, fine needle diathermy and gene therapy targeting VEGF have been widely used in the management of corneal neovascularization (Sharif and Sharif, 2019). Among them, steroids and anti-VEGF agents are currently the mainstay initial treatment approaches. Owing to their low cost and ease of manufacture, steroids (injections and topical treatments)

have become an important alternative in the prevention and treatment of corneal neovascular diseases.

Triamcinolone acetonide (TA), a synthetic steroid, can routinely exerted therapeutic effects in corneal neovascularization through its vasoconstriction and inhibition of inflammation capabilities (Li et al., 2019). Eyedrops, subconjunctival injection, and intraocular injection are the common approaches for TA administration (Jonas et al., 2005; Thorne et al., 2019). However, the natural ocular barriers and the adverse side effects caused by frequent administration limit the applications of these TA ophthalmic solutions, which inspires researchers to develop the alternative TA delivery systems (Singh et al., 2020; Chaw et al., 2021).

In the past decade, hydrogel-based biomaterials attracted significant attention in biomedical science and industrial applications due to their tunable physical, mechanical, and biological characteristics (Luo et al., 2019; Zhu et al., 2020; Clasky et al., 2021). Hydrogels are a form of three-dimensional networks of physically or chemically crosslinked

CONTACT Prof. Hua Gao  hgao@sdfmu.edu.cn; Dr. Hongwei Wang  whw20051256@163.com  State Key Laboratory Cultivation Base, Shandong Provincial Key Laboratory of Ophthalmology, Eye Institute of Shandong First Medical University, Qingdao 266071, China

 Supplemental data for this article can be accessed [here](#).

© 2021 The Author(s). Published by Informa UK Limited, trading as Taylor & Francis Group.

This is an Open Access article distributed under the terms of the Creative Commons Attribution-NonCommercial License (<http://creativecommons.org/licenses/by-nc/4.0/>), which permits unrestricted non-commercial use, distribution, and reproduction in any medium, provided the original work is properly cited.

polymers. Gelatin has been extensively adopted to fabricate hydrogels for biomedical applications such as regenerative medicine (Griffin et al., 2021; Tong et al., 2021), tissue engineering (Park et al., 2020), and drug delivery (Luo et al., 2019; Dou et al., 2020) because of their following attributes: high hydrophilicity, high degree of swelling, excellent biocompatibility, and low immune response. Among these features, the swelling property of hydrogel can to some extent increase biological compatibility; however, it can also cause the mechanical compression of tissues (Ding et al., 2021; M. Zhang et al., 2019). Moreover, low-loading amounts also impeded the wide applications of hydrogels. Thus, it was interesting for researchers to develop hydrogels with a reduced swelling property and an enhanced loading efficiency by chemical modification with functional materials.

Monolith, a kind of porous organic material, is considered as a good stationary phase in the field of chromatographic separations and solid phase extractions (Hong et al., 2016; Zhang et al., 2018). Based on the nature of matrix, monoliths can be mainly classified into silica monoliths and polymeric monoliths (Aggarwal et al., 2012). In recent years, silica-based monoliths have been designed for the construction of drug delivery systems by some researchers (Hernández-Abad et al., 2019; Pudło et al., 2019). Hernández-Abad et al. (2019) fabricated silica monolithic xerogel implants as glibenclamide carriers using the sol-gel technique for subdermal administration. The monolith can achieve a controlled release of glibenclamide; it exhibited its capacity *in vivo* in reducing and maintaining blood glucose levels after administration with a high glucose level in an oral glucose tolerance test. Pudło et al. (2019) synthesized silica monolithic tablets with hierarchical porous structures for a controlled release of tamsulosin. The released profile and the amount of tamsulosin can be adjusted with the tailor-made structures, proving the feasibility of inorganic monolithic materials as a drug delivery system. Polymeric monoliths including polyacrylamides, polymethacrylates, and polystyrenes, could be easily prepared through a single step free radical polymerization and ring-opening polymerization (Kanetkar & Ekenseair, 2020; Khodabandeh et al., 2021; Michl et al., 2020; J. Zhang et al., 2019). To the best of our knowledge, polymeric monoliths have been seldomly used as drug carriers for biomedical diseases (Bender et al., 2020). Thus, the development of polymeric monoliths as alternative drug carriers has the potential for further research.

In this study, we fabricated monolith/hydrogel composites as TA delivery carriers for curing corneal neovascularization. The composites can be synthesized through two steps. Firstly, the monoliths were prepared by a photo-initiated free radical polymerization of multi-methacrylated substituted monomer, which was synthesized by the ring-opening reaction of glycidyl methacrylate (GMA) and dodecamine organic molecular cage (RCC1). Second, the hydrogels were chemically modified onto the surface of the monolith by the photo-initiated free radical polymerization of self-synthesized acrylated gelatin. The as-prepared monolith/hydrogel composites were characterized by scanning electron microscope (SEM), Fourier-transform infrared (FT-IR) spectroscopy, and

solid-state cross polarization magic angle spinning carbon-13 nuclear magnetic resonance (CP-MAS ^{13}C NMR). The TA loading capacity and sustained release properties of the composites were then investigated *in vitro*. Finally, a mouse alkali burn-induced corneal neovascularization model was adopted to study the effect of TA-loaded monolith/hydrogel composite on inhibiting corneal neovascularization, and its mechanism was elucidated by tandem mass tags (TMT)-labeled quantitative proteomics.

2. Materials and method

2.1. Materials and reagents

Gelatin was purchased from Macklin (Shanghai, China). Ethylenediamine, 1,3,5-triformylbenzene (TFB), GMA, and polyethylene glycol (PEG) 10,000 were purchased from Sigma-Aldrich (St Louis, MO, USA). Thermo Fisher Scientific (New Jersey, USA) supplied 2,2-dimethoxy-2-phenylacetophenone (DMPA). Ethanol and NaBH_4 were obtained from the Tianjin Kermel Chemical Reagent plant (Tianjin, China). Methanol and acetonitrile (ACN) were purchased from Merck (Darmstadt, Germany). The Zamboni solution was purchased from Tiandz (Beijing, China). Donkey serum, Triton X-100, Tween-20, Collagenase, and 1x phosphate buffer solution (1x PBS) were obtained from Solarbio (Beijing, China). The syringe (1 mL) was purchased from Hvsco (Beijing, China). Water was purified using a Unique-R20 purification system (Xiamen, China). All reagents and chemicals were at least of analytical grade.

2.2. Preparation of monolith/hydrogel composites

RCC1 was prepared according to the previous method (Culshaw et al., 2013). In brief, the TFB (28.4 mM, 200 mL) methanol solution was slowly added into the ethylenediamine (28.8 mM, 300 mL) methanol solution, which was cooled in an ice bath in a 1 L round-bottomed flask and stirred continuously at 300 r/min. NaBH_4 (0.76 g) was added to the mixture and stirred for 12 h, then H_2O (5.0 mL) was added and the mixture was stirred for another 12 h. RCC1 was purified by chloroform extraction of the concentrate and a white solid was obtained (yield of 86%).

Acetylated gelatin was synthesized according to the protocol reported by Sharifi et al. (2021). First, gelatin (1.0 g) and acrylic anhydride (1.0 mL) were dissolved in 10 mL of PBS (pH 7.5). The mixture was reacted at 50°C for overnight and dialyzed for 5 days against deionized water to remove unreacted monomers. Finally, the dialyzed solution was freeze dried and stored in a refrigerator set at 4°C for further use (Wang et al., 2017).

Monoliths were prepared in the following procedures. RCC1 (16.0 mg), GMA (20.0 μL), methanol (160.0 μL), and PEG10000 (5.0 mg) were mixed and sonicated into a homogeneous solution. The prepared solution was then reacted at 50°C for 4 h. Afterwards, a 10% DMPA ethanol solution (1.0 μL) was added into the solution and the mixture was transferred to a 1 mL syringe covered with sealing film.

The syringe was irradiated under ultraviolet light (365 nm) for 6 min to obtain a white monolith product, which was rinsed with ethanol for at least 6 times.

Acetylated gelatin (2.0% w/v) was weighed and completely dissolved in water to form a uniform and transparent solution. After adding the 10% DMPA (2.0 μ L) ethanol solution, the resulting mixture passed slowly through the monoliths. Subsequently, the monolith was settled under an ultraviolet lamp with a wavelength of 365 nm and irradiated for 15 min. Finally, the monolith/hydrogel composites were taken out from the syringe, rinsed with ethanol for 4 times, lyophilized in a vacuum lyophilizer for over 48 h, and stored in water at 4 °C. In addition, gelatin hydrogel was prepared through a similar method with monolith/hydrogel composite but without monolith.

2.3. Physical characterizations

Monoliths/hydrogel composites and monoliths were ground into powders. SEM images were recorded using an SEM (Gemini SEM 300, Zeiss, Germany). Fourier-transform infrared (FT-IR) spectroscopy was carried out on a Thermo Nicolet 380 spectrometer (Nicolet, Wisconsin, USA) with KBr pellets. CP-MAS ¹³C NMR was obtained using a Bruker Avance III 600 M spectrometer (Bruker Co., Ltd., Switzerland)

2.4. Swelling ratio and loading efficiency

The pre-weighed monolith/hydrogel composites (or gelatin hydrogels) were placed in a centrifuge tube containing PBS (5.0 mL, pH 7.4) to assess the swelling property. At specific time points (0, 1, 2, 3, 6, and 12 h), the samples were taken out, the excess liquid was wiped off, and the samples were weighed. The swelling ratio (*SR*) was calculated using the equation:

$$SR (\%) = (W_c - W_i) / W_i \times 100\%,$$

where W_c and W_i represent the swollen weight and initial weight, respectively.

The same mass of gelatin hydrogels, monoliths and monolith/hydrogel composites were immersed into 10 mL of TA solutions (20 μ g/mL). After 24 h, they were taken out, and the supernatant was detected at 254 nm by HPLC (HPLC operating conditions are listed in Supporting information Figure S1 and Table S1). The TA loading amount (N) was calculated using the equation:

$$N = (C_0 - C_1) \times V,$$

where V represents the volume of TA solution, and C_0 and C_1 represent the concentration of TA solution before and after immersion, respectively. C_0 and C_1 were calculated by the standard curve of TA.

2.5. In vitro drug release and degradability studies

The same mass of monolith/hydrogel composites (about 20.0 mg) were immersed into different concentrations of TA solutions (5 μ g/mL, 10 μ g/mL and 20 μ g/mL, 50 mL),

respectively. After 24 h, three groups of TA-loaded monolith/hydrogel composites were filtered out and added into the PBS solution (4.0 mL). At specific time intervals (0.25, 0.5, 1, 2, 3, 5, 8, 10, 14, 21, and 28 days), 1.0 mL of leaching liquor was withdrawn, and then 1.0 mL of fresh PBS was replenished. The leaching liquor was detected by HPLC, and the TA release curves were drawn by plotting the cumulative amount against time. TA-loaded monolith/hydrogel composites (20.0 μ g/mL) were cut into fixed geometry, and then lyophilized in a vacuum lyophilizer for 48 h for later use.

The *in vitro* degradability of the hydrogels (41.6 ± 0.1 mg), monoliths (24.8 ± 0.8 mg) and composites (25.1 ± 0.6 mg) were investigated by incubating the lyophilized sample in collagenase I-containing (2 U/mL) PBS solution (10.0 mL). At four particular time points (0.5, 1, 2, 4, and 6 days), the samples were taken out, rinsed with the distilled water, and freeze-dried for 24 h.

2.6. In vitro and in vivo biocompatibility studies

DMEM-f12 (Gibco, Grand Island, NY, USA) and 10% FBS (Gibco, Grand Island, NY, USA) were used to prepare a medium suitable for the growth of human corneal epithelium cells (HCECs). Firstly, the monolith/hydrogel composites were placed in a super clean bench and irradiated with an ultraviolet lamp (30 W) for 30 min. Then, sterilized samples (2.5 mg, 5.0 mg, 10.0 mg, and 20.0 mg) were added into the cell culture medium (10.0 mL), respectively and soaked in a constant temperature incubator at 37 °C for 24 h. At last, the monolith/hydrogel composites were filtered out from the cell culture medium, and the extract medium was stored in a refrigerator at 4 °C.

The CCK-8 cell proliferation kit (Yeasen Biotech, Shanghai, China) was used to evaluate the effect of the extract medium on HCECs. The HCECs were seeded into 96-well plates, and the cell count plate was used to adjust the cell number to about 2000 cells/well. The cells were cultured in a cell incubator at 37 °C for 1 day. The culture media in the experimental and control groups were then replaced with the normal medium and pre-prepared extract medium, respectively. After adhesion, HCECs were further cultured in a cell incubator at 37 °C for six consecutive days. At a fixed time each day, in the plates containing HCECs, 10 μ L of CCK-8 reagent were added per well and incubated at 37 °C for 3 h. Then the absorbance was then measured at 450 nm. All experiments were performed with at least three parallel auxiliary holes.

The *in vivo* biocompatibility of the monolith/hydrogel composites was evaluated by subconjunctival implantation of the material in eight-week-old male BALB/c mice. After administering anesthesia through intraperitoneal injection of 3% pentobarbital (1.0 mL/kg), a tiny incision (about 1 mm) was made in mouse conjunctiva. Blunt forceps were used to create a pocket in the subconjunctival space for implanting the composites. The incision was closed with a 11-0 suture (Mani, Tochigi, Japan), and the eyeballs with conjunctiva were harvested at 1, 2, and 4 weeks, respectively.

Hematoxylin and eosin (H&E) staining was performed to examine the histology of subconjunctival tissues at the implanted sites. Briefly, eyeballs were fixed in 4% formalin and embedded in paraffin according to the routing protocol. Continuous 5.0 mm sections were stained with H&E reagents. The slides were then examined and photographed using a light microscope. Immunohistochemistry was performed using a pan-leukocyte marker CD45 (Proteintech, Chicago, USA) to identify the formation of inflammation at the implanted sites. The sections were performed using an automatic immunohistochemical staining machine with primary antibodies CD45 (1:200).

2.7. Corneal alkali burn injury experiments

Eight-week-old male BALB/c mice were anesthetized through an intraperitoneal injection of 3% pentobarbital (1.0 mL/kg), and topically anesthetized with a 0.5% proparacaine hydrochloride solution, respectively. A piece of round filter paper (2.0 mm diameter) was soaked in 1 M NaOH solution, placed on the corneal center for 40 s, and then immediately removed. The mouse eyes were gently flushed with 0.9% normal saline for another 40 s to wash away residual NaOH solution. Alkali-burn mice were divided into four groups ($n = 5$ per group): the blank control group (no any operation), the control group (not processed), the untreated group (implanted with monolith/hydrogel composites), and the treated group (implanted with TA-loaded monolith/hydrogel composites).

The mice were routinely examined in a blinded fashion under a surgical microscope (Table S2) and sacrificed at 10 days for corneal staining and flat mounts. The eyeballs were fixed in Zamboni's solution and then transferred into 10% donkey serum. Rat anti-mouse-PECAM-1 (R&D, AF3628) was applied for detecting blood vessels at 1:200 as the primary antibody, and a 594 nm fluorescent tagged donkey anti-goat-IgG (Invitrogen, A11058) at 1:200 was applied as the secondary antibody. Finally, the cornea was cut into six quadrants of approximately equal size and allowed it to lie flat on a slide with the aid of a surgical microscope. Corneal blood vessels were observed using a fluorescence E800 microscope (Nikon, Tokyo, Japan) and the corneal neovascular area was calculated by the following formula:

$$S = C/12 \times \pi \times [r^2 - (r - L)^2],$$

where S is the area, C is the accumulate hour, L is the radius to the border of the vessel, and r is the radius of the cornea (D'Amato et al., 1994). ImageJ software was used for measuring the radius.

2.8. Tandem mass tags (TMT)-labeled quantitative proteomics

Two corneas were blended as one sample. Mouse corneas from the untreated group ($n = 3$) and the treated group ($n = 3$) were collected for the TMT-labeled quantitative proteomics analysis. The extracted proteins from the corneas were enzymolyzed by trypsin, labeled, and further separated

by reverse-phase HPLC. The segmented samples were analyzed by LC-MS/MS using a Q-Exactive mass spectrometer (Thermo, USA). Experimental conditions: chromatographic column, 75 $\mu\text{m} \times 20$ cm (RP-C18-AQ, ReproSil-Pur); flow rate, 300 $\mu\text{L}/\text{min}$; solvent A, H_2O -FA (99.9:0.1, v/v); and solvent B, ACN- H_2O -FA (80:19.9:0.1, v/v/v). The gradient-elution procedure was used as follows: 0–1 min, 1–6% B; 1–46 min, 6–25% B; 46–52 min, 25–37% B; 52–54 min, 37–95% B; 54–60 min, 95% B.

MS analysis was carried out in full-scan positive ion mode (m/z 375–1800) with the following conditions: mass resolution of first-stage MS, 60000; automatic gain control value, $3e^6$; the maximum injection time, 20 ms; collision energy, 35; MS/MS resolution, 45000; automatic gain control, $2e^5$; the maximum ion injection time, 100 ms; and the dynamic exclusion time, 30 s. Proteome Discover 2.4 (Thermo, USA) was used to screen the credible proteins according to the criteria of Score Sequest HT BBB 0. Unique Peptides ≥ 1 . The volcano plot (gplot2 software package, (version 3.2.2)), cluster analysis map (P heatmap software package, (version 1.0.12)), and the Kyoto Encyclopedia of Genes and Genomes (KEGG) bubble map (GGplot2 software package, (version 3.2.2)) were drawn by an analysis of differential protein expression using R software (version 4.2).

2.9. Statistical analysis

Results collected from at least three independent experiments are reported as mean \pm SD. The statistical analysis was performed by the student's t -test analysis using SPSS 24.0 software. The significance level was set at $p < .05$. Fold change was used to evaluate the variation of the expression level of a certain protein between samples. Fold change equal to 1.2 folds and p value less than .05 were significantly different.

3. Results and discussion

3.1. Synthesis and characterization

The monolith/hydrogel composites were synthesized by sequential photo-initiated free radical polymerization, including the polymerization of methacrylate-substituted RCC1 for fabrication of the monoliths and the subsequent post-modification of monoliths with acrylated gelatin (Figure 1(a–d)). SEM images of both monoliths and monolith/hydrogel composites are shown in Figure 1(e). It can be seen that two monoliths exhibit the typical globular morphology and porous structure of common polymeric monoliths. Figure 1(f) exhibits the FT-IR of GMA, RCC1, monoliths, and monolith/hydrogel composites. The epoxy vibration signal of GMA (908 cm^{-1}) and the secondary amino vibration signal of RCC1 (1661 cm^{-1}) were weakened, indicating that the ring opening reaction between GMA and RCC1 occurred in the formation of multi-methacrylate substituted RCC1. The vibration signal of the double bond (1635 cm^{-1}) in GMA was weakened, and the vibration signal of the carbonyl group shifted from 1720 cm^{-1} in GMA to 1725 cm^{-1} in the monoliths, demonstrating that free radical polymerization occurred in the

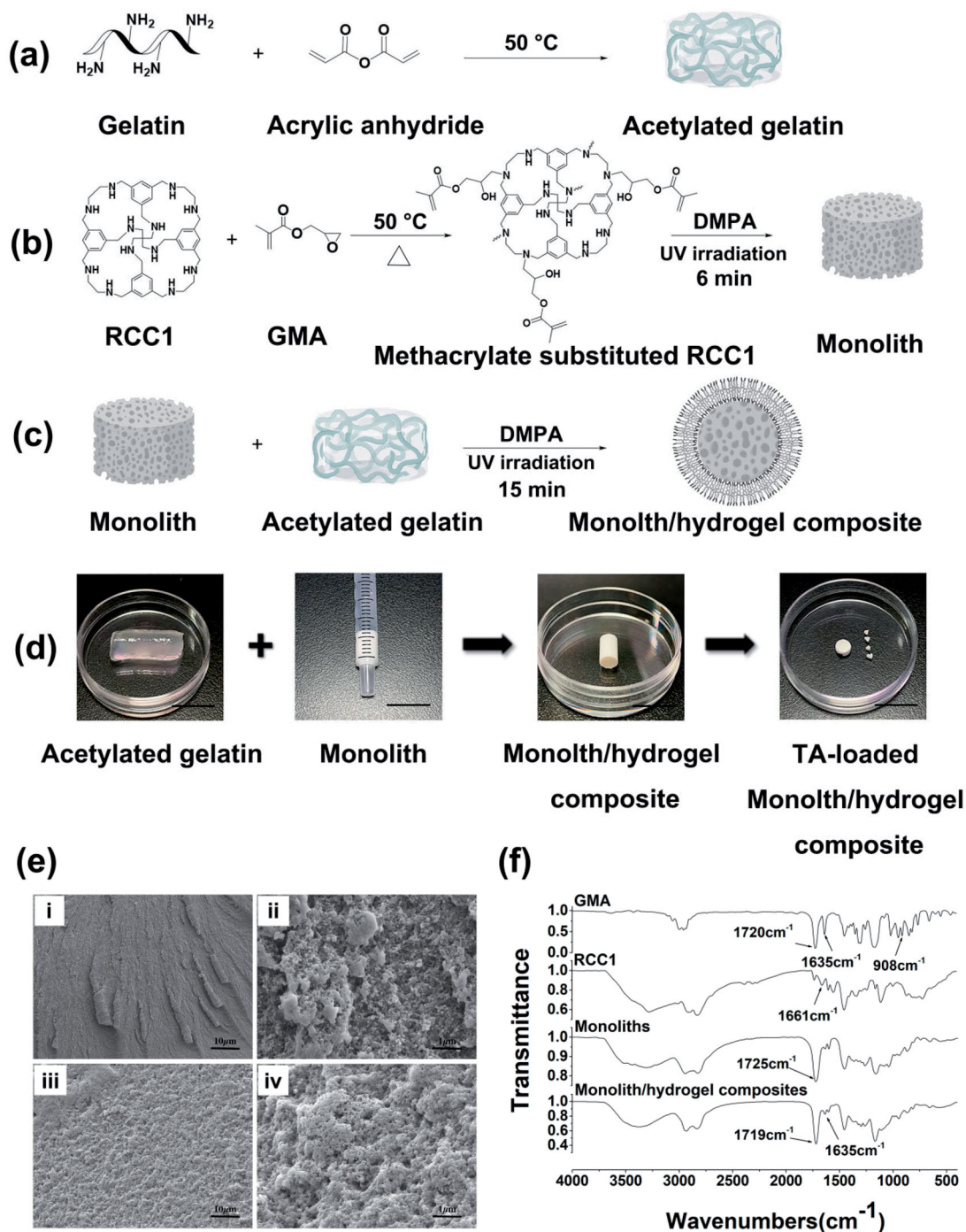


Figure 1. Preparation of (a) the acetylated gelatin, (b) the monoliths, (c) the monolith/hydrogel composites; (d) Pictures of the acetylated gelatin, the monoliths, the monolith/hydrogel composites and the TA-loaded monolith/hydrogel composites. Scale bars, 1.0 cm; (e) SEM of the monoliths (i, ii) and the monolith/hydrogel composites (iii, iv). Scale bars, 10.0 μm (i, iii), 1.0 μm (ii, iv); (f) FT-IR of RCC1, GMA, the monoliths, and the monolith/hydrogel composites.

formation of the monoliths. In the spectrum of monolith/hydrogel composites, the stretching vibration signal (1635 cm^{-1}) was significantly enhanced compared with that of the monoliths due to the introduced free amino group in the gelatin hydrogel post modification. The shifting of the carbonyl signal from 1725 cm^{-1} to 1719 cm^{-1} might be attributed to the incorporation of the ester carboxyl signal in the monolith and carboxylic acid signal in the gelatin hydrogel. Figure S2 (Supporting information) exhibits the solid

state ^{13}C CP MAS NMR spectra of gelatin hydrogel (S2a), monoliths (S2b) and monolith/hydrogel composites (S2c). The ^{13}C -NMR signals δ_{C} 157.5 ppm (aminocarbonyl in hydrogel), δ_{C} 139.8/129.0 ppm (aromatic carbons in monoliths), and δ_{C} 19.0 ppm (methyl in monoliths) were all present in the spectrum of monolith/hydrogel composites, demonstrating the successful incorporation of monoliths and gelatin hydrogel in the composite by sequential photo-initiated free radical polymerization.

3.2. Reduced swelling ratio and improved loading efficiency

The swelling properties of gelatin hydrogels and monolith/hydrogel composites were compared under the same conditions. As shown in Figure 2(a), the swelling ratio significantly decreased in monolith/hydrogel composites ($299.3\% \pm 8.6\%$) compared with gelatin hydrogel ($685.3\% \pm 113.6\%$). In the first hour, the swelling ratio of hydrogels and monolith/hydrogel composites were approximately 9- and 4-fold of the initial weight, respectively. As the time increased to 12 h, there were nearly no changes in the swelling behavior of gelatin hydrogels and monolith/hydrogel composites. Therefore, monolith/hydrogel composites can significantly reduce the swelling capability of gelatin hydrogel.

The TA loading amounts on gelatin hydrogels, monoliths, and monolith/hydrogel composites were investigated by immersing the material into the TA solution ($20.0\ \mu\text{g/mL}$, $10.0\ \text{mL}$) for 24 h. As shown in Figure 2(b,c), the TA loading amounts were found to be $1.7 \pm 0.5\ \mu\text{g}$, $14.6 \pm 0.1\ \mu\text{g}$, and

$17.1 \pm 0.3\ \mu\text{g}$ for gelatin hydrogels, monoliths, and monolith/hydrogel composites, respectively. In addition, the loading efficiencies were also calculated to be 0.84%, 7.28%, and 8.57% for the three groups, which indicates a higher loading efficiency of the monolith/hydrogel composites than gelatin hydrogels. In addition, the TA loading amounts at three concentrations of monolith/hydrogel composites, that is, $5.0\ \mu\text{g/mL}$, $10.0\ \mu\text{g/mL}$, and $20.0\ \mu\text{g/mL}$, were calculated to be approximately $6.1 \pm 2.1\ \mu\text{g}$, $14.4 \pm 2.8\ \mu\text{g}$ and $27.5 \pm 5.6\ \mu\text{g}$, respectively.

3.3. In vitro TA release study

Figure 2(d) displays the *in vitro* TA release profiles of the monolith/hydrogel composites. There was an initial burst of $2.2 \pm 0.4\ \mu\text{g}$, $4.0 \pm 0.4\ \mu\text{g}$ and $7.2 \pm 1.1\ \mu\text{g}$ on the first day in the three groups ($5.0\ \mu\text{g/mL}$, $10.0\ \mu\text{g/mL}$, and $20.0\ \mu\text{g/mL}$), followed by a steadily released amount of drug dose during the next 27 days. After 28 days, the overall release rates were

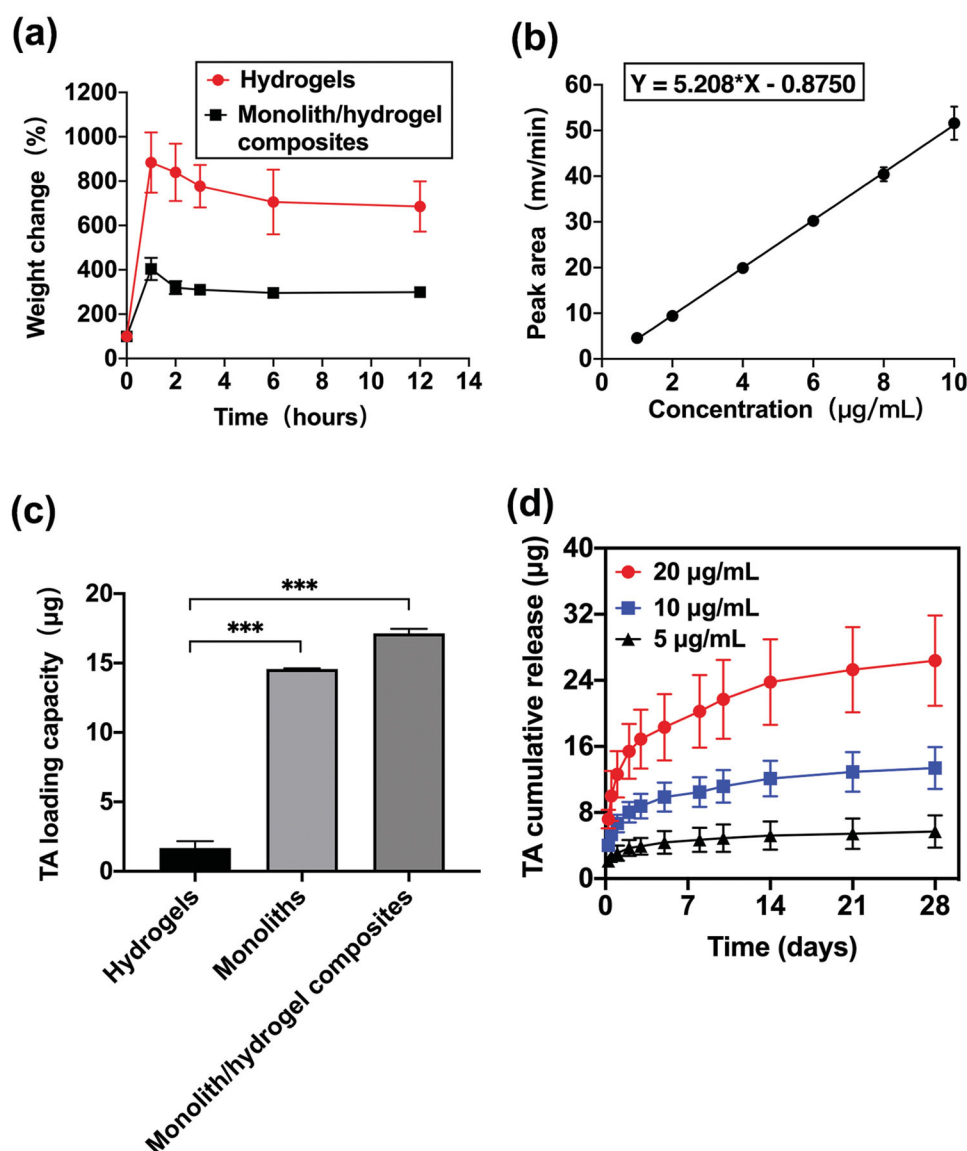


Figure 2. (a) Swelling property of the hydrogels and the monolith/hydrogel composites; (b) Standard curve of TA in PBS; (c) The TA loading amounts in hydrogels, monoliths, and monolith/hydrogel composites; (d) *In vitro* release profile of TA-loaded monolith/hydrogel composites.

above 90.0%. These release curves revealed that TA-loaded monolith/hydrogel composites achieved a steady and sustained release of TA *in vitro*.

3.4. *In vitro/in vivo* biocompatibility and degradability studies

CCK-8 tests were performed to evaluate the cytotoxicity of monolith/hydrogel composites on HCECs *in vitro* (Figure 3(a and b)). After a 6-day culture, the optical density (OD) value was 1.44 ± 0.1 for the control group without the extract medium, whereas 1.32 ± 0.02 (2.5 mg), 1.34 ± 0.08 (5.0 mg), 1.40 ± 0.17 (10.0 mg), and 1.28 ± 0.04 (20.0 mg) for the four experiment groups. The insignificant differences based on

ANOVA results ($p > .05$) indicated that the extract medium did not induce significant changes in cell proliferation compared with negative controls (fresh medium), demonstrating the good *in vitro* biocompatibility of monolith/hydrogel composites.

H&E staining of the eyes ($n = 3$) was used to determine the long-term biocompatibility after subconjunctival implantation of monolith/hydrogel composites at 1, 2, and 4 weeks. Another three sets of normal eyes were selected as the control, which did not undergo the implantation during the observation period. According to H&E staining images (Figure 3(c)), there was no obvious inflammation and edema in the conjunctiva and cornea in the experiment groups. In addition, CD45 staining was performed on the slices to

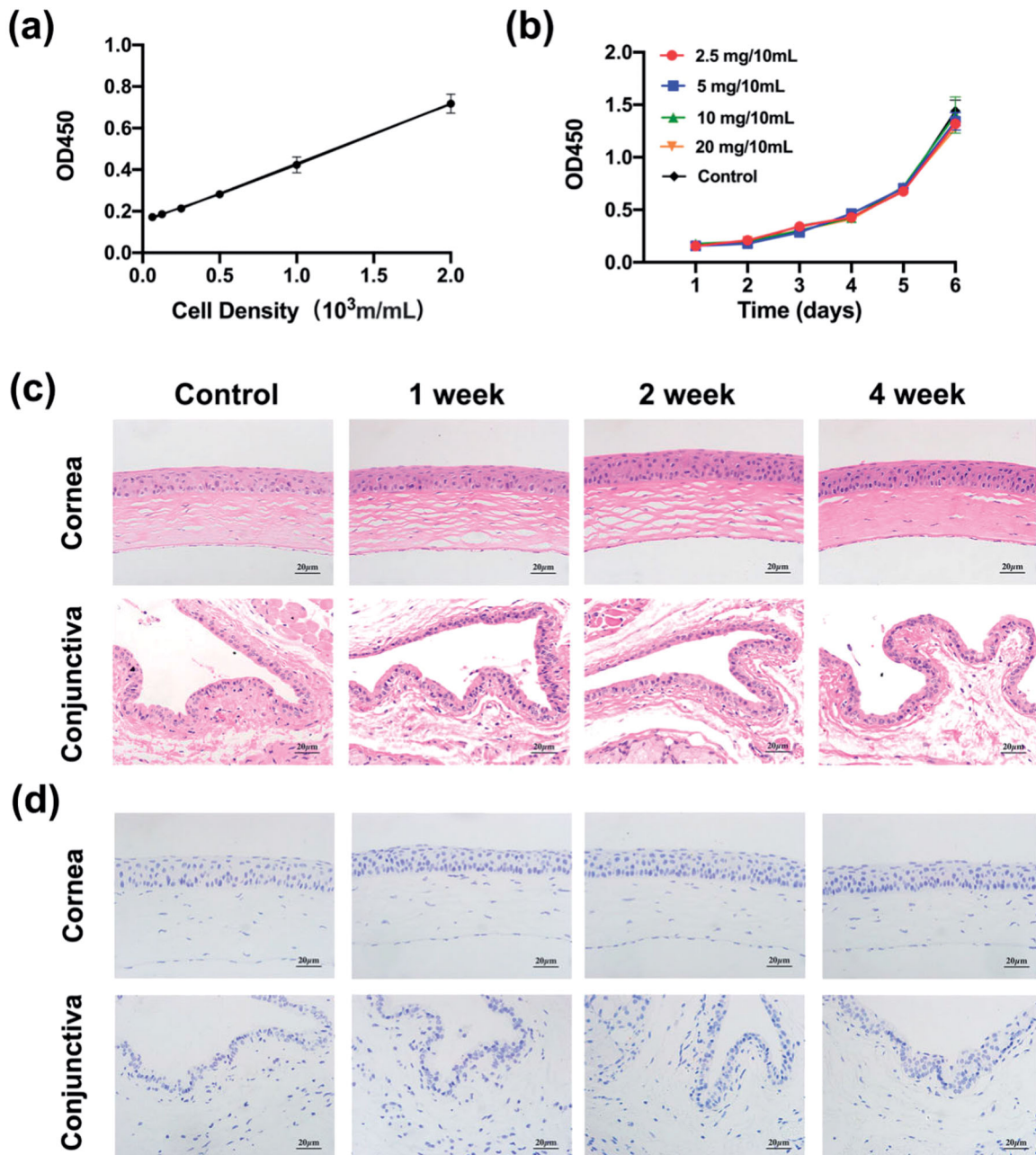


Figure 3. (a) Standard curve of the corneal epithelial cell growth; (b) *In vitro* cytotoxicity of the monolith/hydrogel composites; (c) *In vivo* biocompatibility evaluation of the monolith/hydrogel composites by H&E histology staining of mouse corneas and conjunctivas in the control group and the experimental groups; (d) Anti-CD45 immunohistochemistry staining. Scale bars, 20.0 μm .

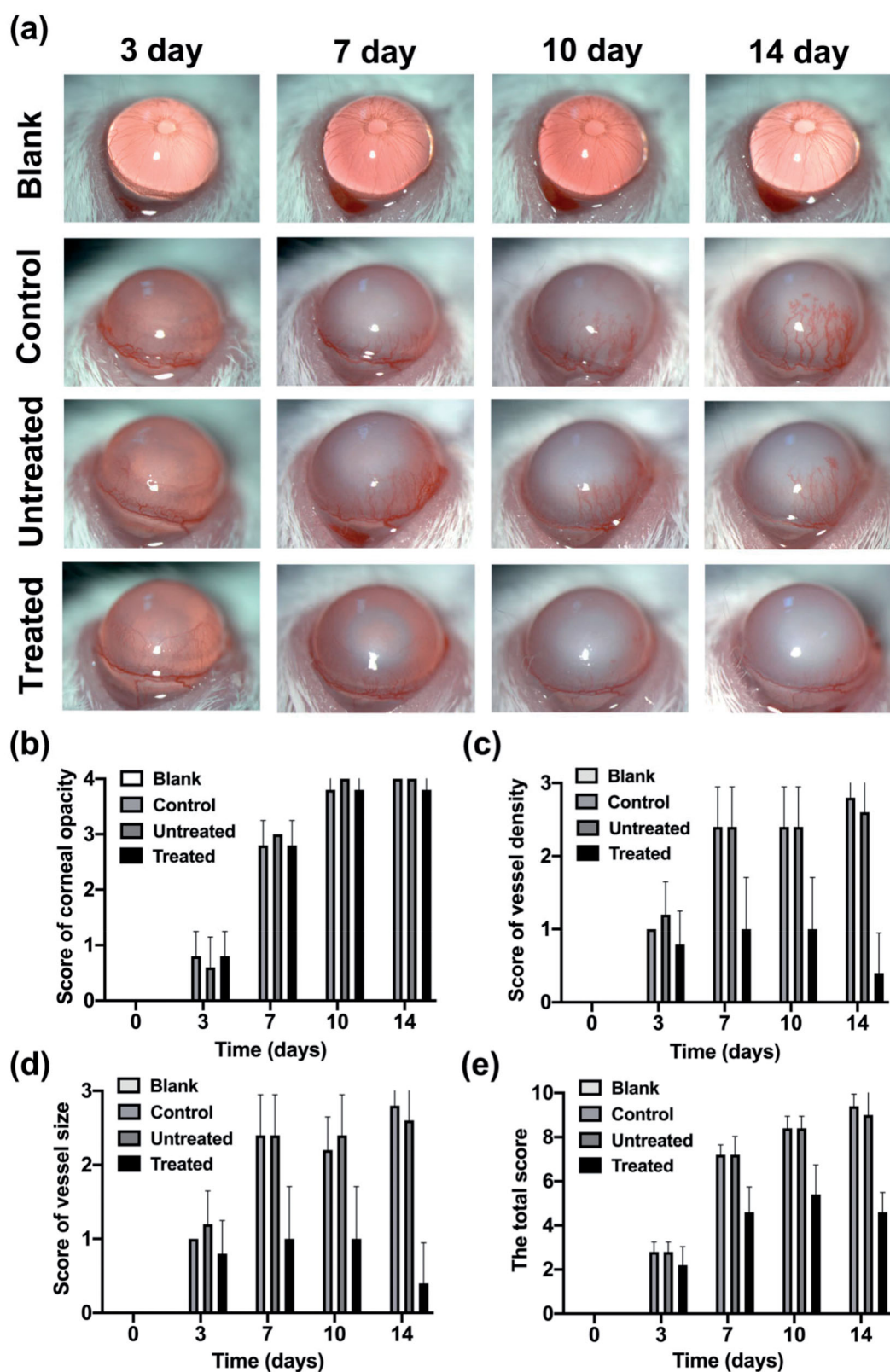


Figure 4. (a) Representative images of corneal neovascularization in alkali burn injury induced mice model at different time points (3, 7, 10, and 14 days); Scores of (b) cornea opacity ($n=5$), (c) vessel density ($n=5$) and (d) vessel size ($n=5$); (e) Total scores of three indicators ($n=5$).

detect the leukocyte and macrophage infiltration after foreign body implantation. The immunohistochemistry results (Figure 3(d)) showed no inflammatory response in both experimental and control groups.

The *in vitro* degradability of the monolith/hydrogel composites was assessed by calculating the mass ratio of the residual composite and total composite. As is shown in Figure S3 (Supporting information), mass percentages of the

hydrogels, the monoliths, and the composites decreased to $67.7\% \pm 9.5\%$, $95.7\% \pm 1.4\%$, and $94.8\% \pm 0.5\%$ at 1 d, respectively. When the immersion time extended to 6 days, hydrogel was almost completely degraded, while there was no significant change in the mass percentages of monolith and the composite, indicating the poor degradability of monolith in the composite. However, it can be stated that the improved loading efficiency and the good biocompatibility allowed the composite to act as a TA carrier on corneal neovascularization. The implantation of sustained TA carriers can afford a long-term therapeutic effect; however, patients would find it difficult to accept the operation, which limits the wide clinical application of the monolith/hydrogel composite. Ophthalmic solutions are an acceptable way for the treatment of eye diseases. However, a high therapeutic concentration was required owing to its low bioavailability, which can cause ocular or even systemic side effects. Thus, further work can be focus on the development of monolith/hydrogel composite based ophthalmic solution for curing corneal neovascularization.

3.5. Inhibiting neovascularization by TA-loaded monolith/hydrogel composites

An alkali-burn injury model was used to evaluate the *in vivo* effect of TA-loaded monolith/hydrogel composites for treating corneal neovascularization. The digital images of the eyes are presented in Figure 4(a). The degrees of corneal opacity (Figure 4(b)), vessel density (Figure 4(c)), and vessel size (Figure 4(d)) were scored for assessing the development of neovascularization, and the total score of the three

indicators is shown in Figure 4(e). Within three days postoperatively, neovascularization in three groups were in the form of growth at the corneal limbus. Subsequently, new blood vessels continued to grow toward the center of the cornea until they crossed the midline of the cornea in the control and untreated groups. The close corneal neovascularization in the control and untreated groups suggested that the composites without TA loading had no therapeutic effect on corneal neovascularization. On the contrary, less vessel growth indicated a considerable suppression of the neovascularization in the treated group when implanted with TA-loaded monolith/hydrogel composites. The extent of corneal neovascularization was evaluated by a quantitative analysis of the vascularized area (Figure 5(b and c)) using corneal staining and flat mounts (Figure 5(a)) at 10 day post operation. The vascularized area in the treated group ($11.5\% \pm 1.8\%$) was significantly smaller than those of the untreated groups ($61.2\% \pm 1.3\%$) and the control group ($61.2\% \pm 3.9\%$) ($p < .05$). These results support the hypothesis that TA-loaded monolith/hydrogel composites are a promising drug delivery system for a sustained release of TA in treating corneal neovascularization.

3.6. Quantitative proteomic analysis of vascularized and devascularized corneas

Figure 6(a) shows the results of the principal component analysis (PCA) between the untreated group and the treated group using the expression level of credible protein. This shows that samples in both groups have satisfactory independence and reproducibility. Subsequently, 210 proteins

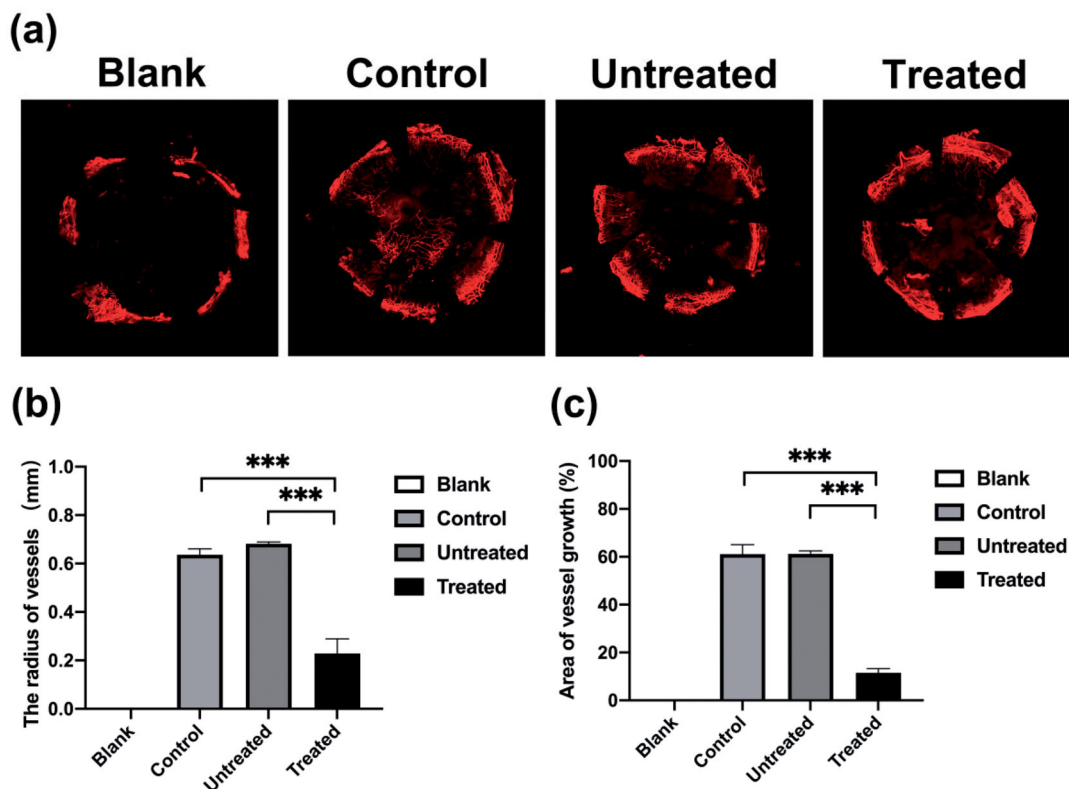


Figure 5. (a) Representative images of corneal staining and flat mounts at 10 day; (b) The radius and (c) the neovascularization area of mouse corneas.

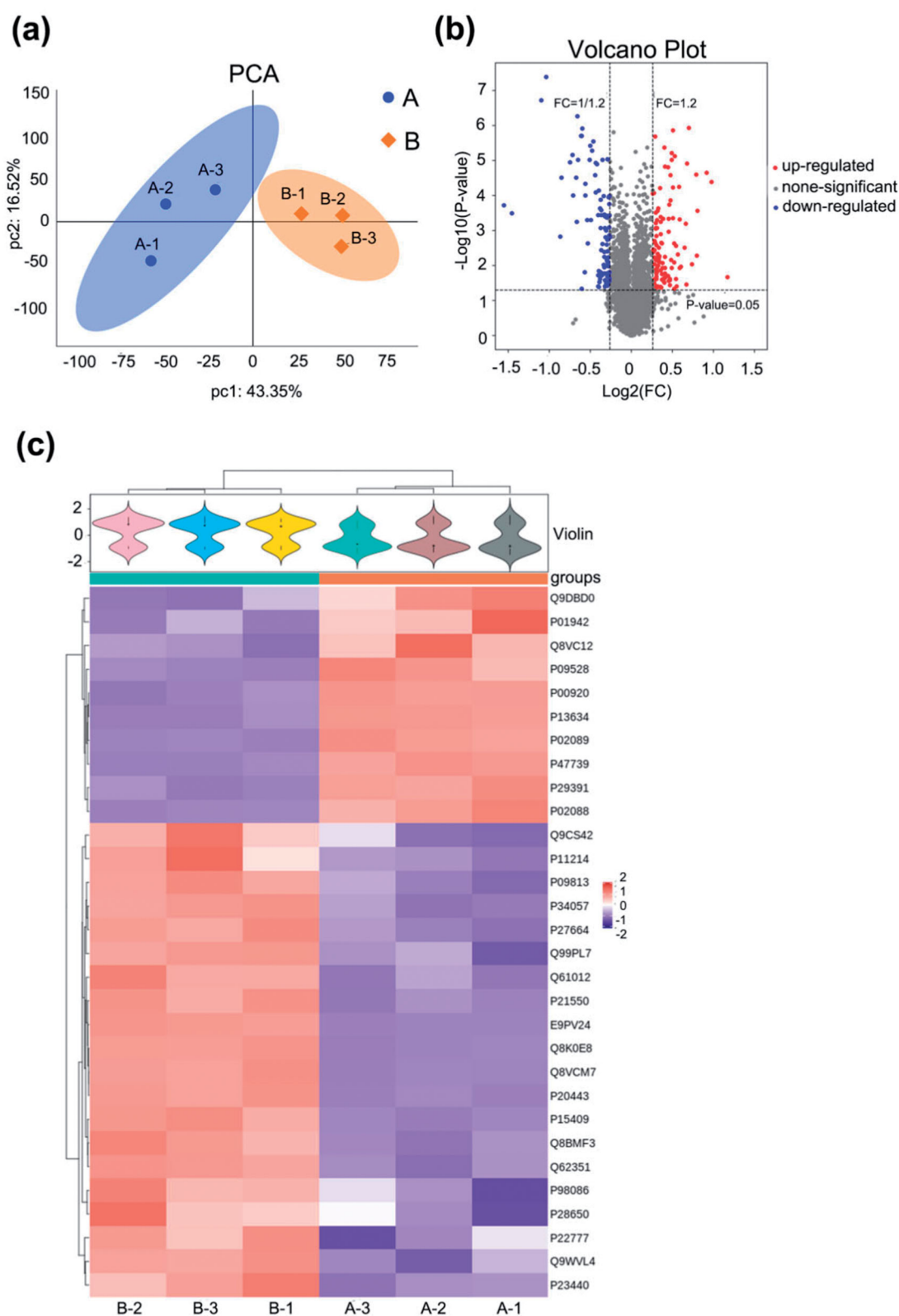


Figure 6. (a) PCA analysis of the expression level of credible proteins from (A) the untreated group and (B) treated group. The further away two coordinate points on the score chart are, the more significant the difference between two groups is; (b) The volcano graph of down-regulated proteins (blue dots), up-regulated proteins (red dots), and non-significantly differentially expressed proteins (gray dots); (c) The heat map according to the protein expression level. Red and blue represent up-regulated and down-regulated proteins, respectively.

with significant differences were obtained by Foldchange, among which 115 proteins were up-regulated and 95 proteins were down-regulated. Visualized volcano maps

(Figure 6(b)) displayed the distribution of up-regulated and down-regulated differential proteins. In addition, 30 proteins ($p < .05$) were further screened out from the 210 differentially

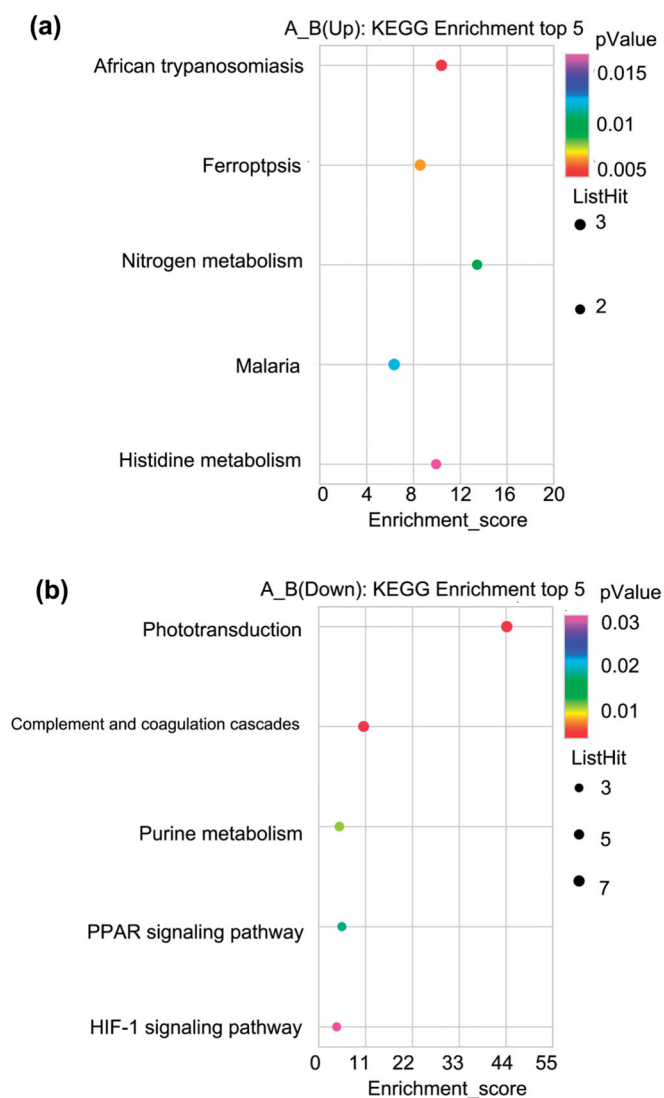


Figure 7. Top five significant KEGG enrichment terms in (a) up-regulated and (b) down-regulated proteins from (A) the untreated group and (B) the treated group. The dot plot illustrated the number of significant genes associated with the first 5 terms (size) and the p -values for these terms (color).

expressed proteins. The corresponding heat map of the cluster analysis is shown in Figure 6(c), indicating the expression levels of different proteins in the untreated group and the treated group.

The KEGG enrichment analysis was performed to describe the functions of differentially expressed proteins. We identified five significant up-regulation pathways and five significant down-regulation pathways that had a p -value of $< .05$ (Figure 7(a and b)). The expressions of *hypoxia inducible factor-1 (HIF-1)*, *peroxisome proliferators-activated receptor (PPAR)*, *complement and coagulation cascades*, *phototransduction* and *purine metabolism* signaling pathways in the untreated group were downregulated, while *ferroptosis*, *nitrogen metabolism*, *histidine metabolism*, *africa trypanosomiasis*, and *malaria* signaling pathways were upregulated, when compared with those in the treated group. Among them, the *HIF-1* signaling pathway was found to be a master regulator of angiogenesis. Previous studies have indicated that *HIF-1* signaling pathway

seems to participate in vascular formation by synergistic correlations with other proangiogenic factors such as VEGF, placental growth factor, or angiopoietins (Iwase et al., 2013; Xu et al., 2018; Wen et al., 2019). *PPAR* signaling pathways were highly correlated with the expression of the genes involved in inflammation (Calvier et al., 2019; Hennigs et al., 2021). The specific mechanism may be realized by the synergistic effect with the co-activator of nuclear receptor after the initial activation and heterodimerization of *PPARs* (Gong et al., 2016). Moreover, a downregulated expression of the *complement and coagulation cascades* signaling pathway may be highly correlated with the inhibition of corneal neovascularization by TA.

Noteworthy, *fibrinogen α chain*, *fibrinogen β chain*, *fibrinogen γ chain*, *tissue-type plasminogen activator (t-PA)*, and *plasminogen activator inhibitor 1 (PAI-1)* were down-regulated in the treated group ($p < .05$), indicating the potential role of the fibrinolytic system in corneal angiogenesis. The components in the plasminogen activation system, including *t-PA*, *urokinase-type plasminogen activator (u-PA)*, *u-PA receptor (u-PAR)*, and *PAI-1*, are involved in physiological and pathological angiogenesis-related disorders, which is in agreement with previous studies (Vogten et al., 2003; Manetti et al., 2014; Colasuonno et al., 2018; Luyendyk et al., 2019). Among them, *PAI-1*, an important serine protease in the fibrinolytic system, may induce and regulate corneal neovascularization independent of its effect on proteolytic activity (Vogten et al., 2003).

In our study, alkali burn may induce mice corneal epithelial cells to secrete *t-PA*, *u-PA*, and other substances. Subsequently, plasminogen in the cornea can be hydrolyzed and activated into plasmin by the action of *t-PA*. Meanwhile, corneal endothelial cells were activated, and secreting proteases including platelet activating factor, matrix metalloproteinases, *PAI-1*, and collagenase (Xu et al., 2020). These proteases dissolved the basement membrane, promoting the migration of endothelial cells and resulting in the formation of new, leaky, and fragile blood vessels in the control group and the untreated group. However, the formation of new vessels was successfully suppressed by TA in the treated group. Although VEGF and annexin A2 have also been reported to be highly correlated with angiogenesis (Liu & Hajjar, 2016; Senturk et al., 2016), we did not find relevant differential proteins in our proteomics data. Therefore, it could be deduced that TA-loaded monolith/hydrogel composites might prevent the occurrence and development of alkali burn-induced corneal neovascularization by inhibiting the fibrinolytic system.

4. Conclusions

In this study, we developed monolith/hydrogel composites as TA delivery systems for inhibiting pathological ocular neovascularization in mice. Monolith/hydrogel composites were fabricated by photo-initiated free radical polymerization of multi-methacrylate substituted RCC1 for preparing of monoliths and the sequential photo-initiated free radical polymerization of acrylated gelatin for the post-modification of

monoliths. The composites exhibited low swelling, high loading amount, and sustained release characteristics compared with gelatin hydrogels. *In vitro* and *in vivo* biocompatibility tests showed that monolith/hydrogel composites exhibited no obvious cytotoxicity to HCECs, the cornea, and the conjunctiva. Alkali-burned mice experiments and tandem mass tags (TMT)-labeled quantitative proteomics revealed that TA-loaded monolith/hydrogel composites exhibit a positive effect on curing the corneal neovascularization by inhibiting the fibrinolytic system. It could be anticipated that monolith/hydrogel composites possessed the potential to act as a suitable drug delivery system for therapeutical applications in other biomedical diseases.

Acknowledgments

All animal studies were performed in accordance with the Association for Research in Vision and Ophthalmology Statement for the Use of Animals in Ophthalmic and Vision Research. The experiments were approved by the Medical Ethics Committee of Shandong Eye Institute, China. We are thankful to BioRender.com for providing us with figure materials.

Disclosure statement

The authors declare that they have no known competing financial interests or personal relationships that could have appeared to influence the work reported in this paper.

Funding

This study was supported by National Natural Science Foundation of China [82070923, 81870639], Taishan Scholar Program [201812150, 20150215], and the Academic Promotion Program and Innovation Project of Shandong First Medical University [2019RC009].

ORCID

Xiaolin Qi  <http://orcid.org/0000-0003-4410-3178>

References

- Aggarwal P, Tolley HD, Lee ML. (2012). Monolithic bed structure for capillary liquid chromatography. *J Chromatogr A* 1219:1–14.
- Bender L, Boostrom HM, Varricchio C, et al. (2020). A novel dual action monolithic thermosetting hydrogel loaded with lidocaine and metronidazole as a potential treatment for alveolar osteitis. *Eur J Pharm Biopharm* 149:85–94.
- Calvier L, Boucher P, Herz J, et al. (2019). LRP1 deficiency in vascular SMC leads to pulmonary arterial hypertension that is reversed by PPAR γ activation. *Circ Res* 124:1778–85.
- Chaw SY, Novera W, Chacko AM, et al. (2021). *In vivo* fate of liposomes after subconjunctival ocular delivery. *J Control Release* 329: 162–74.
- Cho W, Mittal SK, Elbasiony E, et al. (2020). Activation of ocular surface mast cells promotes corneal neovascularization. *Ocul Surf* 18: 857–64.
- Clasky AJ, Watchorn JD, Chen PZ, et al. (2021). From prevention to diagnosis and treatment: biomedical applications of metal nanoparticle-hydrogel composites. *Acta Biomater* 122:1–25.
- Colasuonno M, Palange AL, Aid R, et al. (2018). Erythrocyte-inspired discoidal polymeric nanoconstructs carrying tissue plasminogen activator for the enhanced lysis of blood clots. *ACS Nano* 12:12224–37.
- Culshaw JL, Cheng G, Schmidtman M, et al. (2013). Dodecaamide cages: organic 12-arm building blocks for supramolecular chemistry. *J Am Chem Soc* 135:10007–10.
- D'Amato RJ, Loughnan MS, Flynn E, et al. (1994). Thalidomide is an inhibitor of angiogenesis. *Proc Natl Acad Sci USA* 91:4082–5.
- Ding H, Li B, Liu Z, et al. (2021). Nonswelling injectable chitosan hydrogel via UV crosslinking induced hydrophobic effect for minimally invasive tissue engineering. *Carbohydr Polym* 252:117143.
- Dou Y, Li C, Li L, et al. (2020). Bioresponsive drug delivery systems for the treatment of inflammatory diseases. *J Control Release* 327:641–66.
- Gong Y, Shao Z, Fu Z, et al. (2016). Fenofibrate inhibits cytochrome p450 epoxygenase 2C activity to suppress pathological ocular angiogenesis. *EBioMedicine* 13:201–11.
- Griffin DR, Archang MM, Kuan CH, et al. (2021). Activating an adaptive immune response from a hydrogel scaffold imparts regenerative wound healing. *Nat Mater* 20:560–9.
- Hennigs JK, Cao A, Li CG, et al. (2021). PPAR γ -p53-mediated vasculoregenerative program to reverse pulmonary hypertension. *Circ Res* 128: 401–18.
- Hernández-Abad VJ, Sánchez-González EG, Espinosa-Contreras C, et al. (2019). Controlled release of glibenclamide from monolithic silica subdermal implants produced by the sol-gel process and its use for hyperglycaemia treatment in a murine model. *Mater Sci Eng C Mater Biol Appl* 94:1009–19.
- Hong T, Yang X, Xu Y, et al. (2016). Recent advances in the preparation and application of monolithic capillary columns in separation science. *Anal Chim Acta* 931:1–24.
- Iwase T, Fu J, Yoshida T, et al. (2013). Sustained delivery of a HIF-1 antagonist for ocular neovascularization. *J Control Release* 172: 625–33.
- Jonas JB, Kreissig I, Degenring R. (2005). Intravitreal triamcinolone acetate for treatment of intraocular proliferative, exudative, and neovascular diseases. *Prog Retin Eye Res* 24:587–611.
- Kanetkar NS, Ekenseair AK. (2020). Thiolated thermoresponsive polymer scaffolds with tunable mucoadhesivity for intestinal applications. *Biomacromolecules* 21:4761–70.
- Khodabandeh A, Arrua RD, Thickett SC, et al. (2021). Utilizing RAFT polymerization for the preparation of well-defined bicontinuous porous polymeric supports: application to liquid chromatography separation of biomolecules. *ACS Appl Mater Inter* 13:32075–83.
- Li J, Cheng T, Tian Q, et al. (2019). A more efficient ocular delivery system of triamcinolone acetate as eye drop to the posterior segment of the eye. *Drug Deliv* 26:188–98.
- Liu W, Hajjar KA. (2016). The annexin A2 system and angiogenesis. *Biol Chem* 397:1005–16.
- Luo Z, Sun W, Fang J, et al. (2019). Biodegradable gelatin methacryloyl microneedles for transdermal drug delivery. *Adv Healthc Mater* 8: e1801054.
- Luyendyk JP, Schoenecker JG, Flick MJ. (2019). The multifaceted role of fibrinogen in tissue injury and inflammation. *Blood* 133: 511–20.
- Manetti M, Rosa I, Milia AF, et al. (2014). Inactivation of urokinase-type plasminogen activator receptor (uPAR) gene induces dermal and pulmonary fibrosis and peripheral microvasculopathy in mice: a new model of experimental scleroderma? *Ann Rheum Dis* 73: 1700–9.
- Michl TD, Hibbs B, Hyde L, et al. (2020). Bacterial membrane permeability of antimicrobial polymethacrylates: evidence for a complex mechanism from super-resolution fluorescence imaging. *Acta Biomater* 108: 168–77.
- Park SH, Park JY, Ji YB, et al. (2020). An injectable click-crosslinked hyaluronic acid hydrogel modified with a BMP-2 mimetic peptide as a bone tissue engineering scaffold. *Acta Biomater* 117:108–20.
- Pudło W, Borys P, Huszcza G, et al. (2019). Hierarchical silica monolithic tablets as novel carriers for drug delivery. *Eur J Pharm Biopharm* 141: 12–20.

- Senturk B, Cubuk MO, Ozmen MC, et al. (2016). Inhibition of VEGF mediated corneal neovascularization by anti-angiogenic peptide nanofibers. *Biomaterials* 107:124–32.
- Sharif Z, Sharif W. (2019). Corneal neovascularization: updates on pathophysiology, investigations & management. *Rom J Ophthalmol* 63: 15–22.
- Sharifi S, Islam MM, Sharifi H, et al. (2021). Tuning gelatin-based hydrogel towards bioadhesive ocular tissue engineering applications. *Bioact Mater* 6:3947–61.
- Singh M, Bharadwaj S, Lee KE, et al. (2020). Therapeutic nanoemulsions in ophthalmic drug administration: concept in formulations and characterization techniques for ocular drug delivery. *J Control Release* 328:895–916.
- Thorne JE, Sugar EA, Holbrook JT, et al. (2019). Periocular triamcinolone vs. intravitreal triamcinolone vs. intravitreal dexamethasone implant for the treatment of uveitic macular edema: the periocular vs. intravitreal corticosteroids for uveitic macular edema (POINT) trial. *Ophthalmology* 126:283–95.
- Tong Z, Jin L, Oliveira JM, et al. (2021). Adaptable hydrogel with reversible linkages for regenerative medicine: dynamic mechanical micro-environment for cells. *Bioact Mater* 6:1375–87.
- Ueta T, Ishihara K, Notomi S, et al. (2019). RIP1 kinase mediates angiogenesis by modulating macrophages in experimental neovascularization. *Proc Natl Acad Sci USA* 116:23705–13.
- Vogten JM, Reijkerker A, Meijers JC, et al. (2003). The role of the fibrinolytic system in corneal angiogenesis. *Angiogenesis* 6:311–6.
- Wang Z, Liu CH, Huang S, et al. (2019). Wnt Signaling in vascular eye diseases. *Prog Retin Eye Res* 70:110–33.
- Wang Z, Tian Z, Menard F, et al. (2017). Comparative study of gelatin methacrylate hydrogels from different sources for biofabrication applications. *Biofabrication* 9:044101.
- Wen Y, Zhou X, Lu M, et al. (2019). Bclaf1 promotes angiogenesis by regulating HIF-1 α transcription in hepatocellular carcinoma. *Oncogene* 38:1845–59.
- Xu J, Zhang Y, Xu J, et al. (2020). Engineered nanoplatelets for targeted delivery of plasminogen activators to reverse thrombus in multiple mouse thrombosis models. *Adv Mater* 32:e1905145.
- Xu Y, Lu X, Hu Y, et al. (2018). Melatonin attenuated retinal neovascularization and neuroglial dysfunction by inhibition of HIF-1 α -VEGF pathway in oxygen-induced retinopathy mice. *J Pineal Res* 64:e12473.
- Zhang J, Chen J, Peng S, et al. (2019). Emerging porous materials in confined spaces: from chromatographic applications to flow chemistry. *Chem Soc Rev* 48:2566–95.
- Zhang M, Chen S, Sheng N, et al. (2019). A strategy of tailoring polymorphs and nanostructures to construct self-reinforced nonswelling high-strength bacterial cellulose hydrogels. *Nanoscale* 11:15347–58.
- Zhang S, Yang Q, Wang C, et al. (2018). Porous organic frameworks: advanced materials in analytical chemistry. *Adv Sci (Weinh)* 5: 1801116.
- Zhu Y, Ma Z, Kong L, et al. (2020). Modulation of macrophages by bio-active glass/sodium alginate hydrogel is crucial in skin regeneration enhancement. *Biomaterials* 256:120216.